Novel miniaturised microbial electrosynthesis reactor

A study on replicability

Zegers, Marika A.J.; Augustijn, Eva; Jongbloed, Geurt; Jourdin, Ludovic

DOI
10.1016/j.cej.2025.163881

Publication date
2025

Document Version
Final published version

Published in
Chemical Engineering Journal

Chemical Engineering Journal 516 (2025) 163881

Contents lists available at ScienceDirect

Chemical Engineering Journal

journal homepage: www.elsevier.com/locate/cej

Novel miniaturised microbial electrosynthesis reactor: A study on replicability☆

Marika A.J. Zegers [a], Eva Augustijn [a], Geurt Jongbloed [b], Ludovic Jourdin [a,*,1]

[a] Department of Biotechnology, Delft University of Technology, van der Maasweg 9, 2629 HZ Delft, the Netherlands
[b] Delft Institute of Applied Mathematics, Delft University of Technology, Mekelweg 4, 2628 CD Delft, the Netherlands

ARTICLE INFO

Keywords:
Microbial electrosynthesis
CO_2 reduction
Reactor design
Replicability
Micro-CT
Biofilm
Carboxylic acids

ABSTRACT

Carbon capture and utilisation are crucial for reducing fossil fuel dependence and transforming the chemical and energy industries. Microbial electrosynthesis (MES) is a promising technology where electrotrophic microorganisms convert CO_2 into valuable biochemicals using electricity. Despite recent advancements, replicability in MES remains poorly understood, with scarce pre-inoculation abiotic data and limited exploration of abiotic and biotic performance correlations. This study introduces a novel miniaturised reactor, modelled after a state-of-the-art flat-plate directed-flow-through bioelectrochemical reactor (DFBR). Four miniaturised reactors were tested in parallel under abiotic conditions to evaluate the impact of electrode material, reactor design, and assembly on replicability of electrochemical behaviour. Using the dynamic time warping (DTW) algorithm, reactor similarity was quantified for the first time based on electrochemical performance. Kernel scatterplot smoothing on micro-CT data revealed that electrodes, particularly the commonly used carbon felt, are a significant source of variability in electrochemical performance, as further supported by additional abiotic electrochemical tests. Additionally, the miniaturised reactors were inoculated with an enriched mixed culture to examine microbial activity's effect on replicability, achieving concentrations up to 4.55 g L^{-1} acetate, 0.96 g L^{-1} butyrate, and 0.38 g L^{-1} caproate after 60 days. Variations in abiotic conditions, including maximum reachable current density, onset potential, and porosity, influence biofilm growth and performance. The miniaturised DFBR effectively represents the serpentine DFBR, while the adaptable reactor design and proposed statistical methods set a new benchmark for MES research.

1. Introduction

Converting carbon dioxide (CO_2) into valuable chemicals, fuels, and feed, known as carbon capture and utilization (CCU), is a critical strategy for global defossilisation and reshaping the chemical, energy and feed industries [1]. The outlook of a chemical industry centred around renewable feedstock and electrical energy is an attractive prospect to many societal, industrial and government stakeholders [2]. Microbial electrosynthesis (MES) is a promising technology to meet the growing demand for both commodity and specialty chemicals, while also enhancing the value of electrical energy generated from renewable sources [3]. MES involves the utilisation of electrotrophic microorganisms to drive the reduction of CO_2 into valuable biochemicals (e.g. carboxylates and alcohols) using electrons provided by a solid-state electrode [4,5]. Either bacteria in suspension or a biofilm on the cathode surface catalyse the production of biochemicals in MES [4,6,7]. To date, the highest production rates of carboxylates (acetate, butyrate and caproate) have been achieved in an MES cell using a 3D structured electrode, which allowed the formation of a uniform biofilm throughout the electrode [8,9].

In biofilm-driven, continuously operated MES, an electrolyte flowing through a porous electrode matrix has been shown to result in higher current densities and improved biofilm coverage, higher microbial activity and higher overall productivity [6,10]. Despite these advances, the potential industrial application of such a reactor configuration continues to be hampered by the knowledge gaps on microbial metabolism and multiple operating conditions. Furthermore, while these systems have showcased notable carboxylate production rates, the

☆ This article is part of a special issue entitled: 'Beyond the Horizon of MET' published in Chemical Engineering Journal.

* Corresponding author.
E-mail address: l.jourdin@tudelft.nl (L. Jourdin).
[1] Lead Contact.

https://doi.org/10.1016/j.cej.2025.163881

Available online 18 May 2025

experiments remain characterised by extended durations. In the context of carboxylate production, numerous recent studies report the observation of caproate production only after 150 days [8,11,12]. The development of scalable reactor designs undeniably provides profound insights into the potential performance of the technology on a macroscale [9,12–16]. However, these reactor systems are not suitable for rapidly screening optimal operating conditions and expediting experiments. Given the demand for a better understanding of the underlying phenomena that drive MES, the utilisation of small, or miniaturised, reactor designs could be a viable way to provide these essential insights. Miniaturised MES could enable crucial research into these processes in a smaller biofilm with better control over the microenvironment. It is important to emphasise that these miniaturised reactors must enable research into phenomena relevant to larger, scalable reactor systems.

For microbial fuel cells (MFCs), extensive research has already been dedicated to the implementation of miniaturised reactors, although for reasons that may not be directly applicable to MES. Existing literature highlights miniaturised MFCs as a more effective approach to producing electricity, making them relevant for powering small devices (e.g. sensors) or stack assemblages [17–19]. In a microliter-sized MFC, the substrate availability on the established biofilm is significantly increased, thereby improving the mass transfer flux of the substrate from the solution to the anode [20]. Furthermore, reducing the size of an MFC leads to a weakening of the large-scale pH gradient, a property that is undesirable for larger MFCs [21,22]. However, it is important to note that MFCs operate under fundamentally different conditions to MES systems: MFCs are designed to generate power via anodic oxidation, whereas MES requires continuous external energy input to drive reductive processes at the cathode. As such, the operating mode, electron flow direction, and performance targets differ considerably, thus requiring largely different design concepts.

For bioelectrochemical systems (BESs) in general, tremendous progress has been made towards the screening of electroactive organisms. To facilitate the development of novel technologies using (genetically engineered) electroactive bacteria, there is a need for miniaturised arrays that can assess the electrochemical attributes of a variety of electroactive bacterial strains within a short timeframe. In a publication by Yates et al. [23], an adapted eight-chamber nanolitre-scale electrochemical flow cell was used to grow biofilms of various electroactive bacteria on electrodes held at a constant potential. The research compared the performance of unmodified strains in nano- and millilitre-scale reactors and found similar maximum current densities. Work by Molderez et al. [24] took a different approach and developed a 128-channel potentiostat connected to a 128-gold electrode array, allowing simultaneous electrochemical measurements with independent electrical signal inputs. The research assessed the impact of 11 different electrode potentials on the growth and electrochemical characteristics of anodic electroactive biofilms formed by microbial communities. Unlike these existing methods for screening electroactive organisms, a device presented in a recent study can simulate a gas-fed and mediator-based BES [25]. It uses 3.5 mL cuvettes as reaction vessels with commercially available screen-printed electrodes and a photometer equipped with an autosampler to measure cell density and mediator redox state in real-time. This setup achieved relatively high current densities and significantly reduces experimental times compared to traditional bioelectrochemical reactor systems, making it a valuable tool for fundamental research in this field.

The nano- to millilitre scale, membrane-less, reactors presented in the aforementioned studies play a crucial role in accelerating the electrochemical characterisation of natural and genetically engineered electroactive microorganisms, as they can provide valuable insights into the behaviour of microorganisms under controlled conditions. However, it is important to recognise that these reactors do not accurately represent scalable reactor designs nor are they intended for evaluating operating conditions relevant to larger-scale biofilm-driven MES systems. For instance, Roman-Casas et al. employed the Micro Flow Cell (ElectroCell Europe, Denmark), featuring carbon felt electrodes with a projected surface area of 10 cm^2 and 3–4 mL chamber volumes, in a study on selective butyric acid production from CO_2 [26]. While this system enables flexible small-scale operation and is suitable for screening different chemicals, electrodes, and membrane materials, its parallel-plate geometry does not reflect the flow-through, porous-electrode configurations used in recent scalable MES reactor designs [9,16]. This highlights a notable gap in the current MES research landscape, namely the lack of a small-scale reactor system that bridges the gap between miniaturised reactors and the practical requirements of larger-scale operations.

Another area that requires further exploration in the MES research field is the study of data replicability across multiple reactors, which ideally should show consistent trends. While several significant studies have presented the performance metrics (e.g. production rates) of multiple reactors, the underlying reasons for variations between reactors' performance have not been thoroughly addressed [8,12,27–32]. Moreover, there is a significant lack of research on abiotic behaviour, particularly on the electrochemical responses of the system, which often remain disconnected from the observed cell performance following inoculation.

In this study, a miniaturised directed-flow-through bioelectrochemical reactor (DFBR) with a total volume of only 1 cm^3 is presented, which is representative of a larger DFBR design proposed by Cabau-Peinado et al. [9]. This larger DFBR achieved a three-times denser biofilm, volumetric current density, and productivity compared with the previous state of the art. Following the work of Cabau-Peinado et al., Deutzmann et al. also demonstrated high performance using a similar serpentine DFBR [16]. Like the serpentine DFBR, the miniaturised design features a channel completely filled with a porous 3D carbon-based electrode and no free-flowing liquid in the cathode chamber. The design presented here mirrors the flow-through geometry of the serpentine DFBR, allowing for more targeted, resource-efficient, and time-efficient investigation of this scalable concept under well-controlled conditions. While the miniaturised DFBR itself is not intended for scale-up, it was specifically designed to be representative of the larger, scalable serpentine DFBR. This allows key performance indicators such as biomass-specific growth rates, biofilm coverage, and product formation to be assessed under comparable conditions, while enabling faster and more resource-efficient experimentation. To gain deeper insight into the replicability of this novel system, the electrodes and reactors were abiotically characterised using micro-CT imaging and conventional electrochemical techniques followed by statistical analysis. Following inoculation, the biofilm that developed on the cathode demonstrated the ability to produce C2, C4, and C6 carboxylic acids. This comprehensive data set highlights the potential of the miniaturised DFBR design to provide deeper insights into the phenomena driving scalable MES processes. It should be noted that the aim of this work was not to demonstrate replicability, but rather to explore current limitations in replicability within MES research and propose strategies to better address them.

2. Materials and methods

2.1. Cathode assembly and micro-CT imaging

Unmodified carbon felt was used as the cathode electrode material (CTG Carbon GmbH, Germany). Before cutting, the felt was cleaned with 1 M HCl (24 h) and 1 M NaOH (24 h). After this treatment step, 25 pieces of carbon felt with the following dimensions were cut: 5 mm × 6 mm × 40 mm. Ten pieces with corresponding weights (average weight 0.145 g) were selected for plasma treatment with compressed air (Plasma Cleaner PDC-002-HPCE, Harrick Plasma, USA) for 30 min. After plasma treatment, 6 electrodes were selected. The carbon felt was then attached to a 6 mm × 5 mm × 40 mm graphite plate (Fuel Cell Store, USA) with a 3 mm wide layer of conductive coating (Graphite Conductive Adhesive,

Electron Microscopy Sciences, USA) to improve the electric connection between both parts. This process involved applying 1 mm-wide strips of tesa® standard masking tape along both edges of the 5 mm side of the graphite plate. A thick layer of graphite conductive adhesive was then applied over the exposed area and any excess adhesive was carefully removed with a spatula to achieve a uniform layer of the paint. After the tape was removed, the carbon felt was positioned on top of the adhesive-coated graphite plate. To ensure proper contact and slight pressure between the layers, a Schott bottle cap was placed on top.

Micro-CT imaging was used to gain insight into the structure and porosity of carbon felt electrodes. Before scanning, the graphite plate with carbon felt attached was glued to a cylindrical glass rod. Once the scan was complete, the sample was removed from the glass rod and returned to the Petri dish where it was stored. The images were acquired with a TESCAN CoreTOM Micro CT (TESCAN GROUP, Czech Republic) with X-rays at 80 kV. The voxel size used was 25 μm. Image analysis of the micro-CT scans and determination of electrode porosities were performed in Dragonfly (version 2022.2.0.1409).

2.2. Miniaturised reactor design

Several design considerations had to be made whilst developing the miniaturised DFBR, as it had to represent the larger serpentine DFBR proposed by Cabau-Peinado et al. [9]. In addition, the reactor design had to be adaptable to enable other experiments (e.g. imaging) in the future. Key design features that had to be translated to a miniaturised scale included: (1) dimensions of the serpentine DFBR channel, (2) direct flow through the 3D/fibrous electrode, (3) graphite plate current collector connected to the carbon felt electrode with graphite adhesive, (4) the reference electrode. To mimic the dimensions of the serpentine DFBR channel, a section of the flow pattern was taken that had a height of 0.5 mm and a width of 5.429 mm. These were translated into similar dimensions (height 0.5 mm and width 5 mm) on the miniaturised reactor (Fig. 1). By also translating the recirculation rate from the larger reactor to the smaller-scale system, it was expected to achieve similar fluid dynamics (see Section 2.3). The miniaturised reactor's bubble column was also resized to be more compatible with smaller volumes while still allowing gas to bubble through, being able to accommodate a total of 30 mL of liquid.

To connect the carbon felt and graphite plate to the potentiostat, a different method was used than in the serpentine DFBR, where a square graphite plate was glued to the serpentine carbon felt with graphite adhesive. In this work, a titanium (Ti) rod was screwed into the graphite plate to ensure a good connection between all the different parts and to minimise the number of parts to be stacked.

Just like the serpentine DFBR, the reference electrode was placed in the catholyte flow directly after the electrode chamber. To prevent gas accumulation around the reference electrode, which can distort the probe's signal, the reference electrode was placed in a dome-shaped chamber to ensure efficient removal of gas bubbles.

2.3. MES reactor setup

Four bioelectrochemical reactors were assembled and operated abiotically (R1, R2, R3, R4). Each reactor consisted of a cathode and anode compartment, with a cation exchange membrane (CEM) (CMI-7000 s, Membrane International Inc.) and an NBR O-ring (50.52 mm x 1.78 mm) separating the two. A schematic of the reactor setup can be found in Fig. 2. Exact reactor dimensions are provided in S1. All reactor parts were 3D-printed using a biocompatible resin (BioMed Clear Resin V1, Formlabs) and the Form 3B printer (Formlabs). The total volume of the carbon felt cathode in the reactor was 1 cm^3, with a projected surface area of 2 cm^2. A Ti plate coated with Pt/IrO_2 (Magneto Special Anodes, Schiedam, The Netherlands) was used as anode material.

To sparge a mixture of CO_2 and N_2 into the catholyte, a bubble column was installed in the recirculation loop, which was also 3D-printed. To regulate the pH of the catholyte to 5.4, a pH controller (AQUIS touch S, Jumo) connected to a pH probe (QP108X, ProSense, The Netherlands) placed in the catholyte recirculation circuit was used. The total volume of the catholyte in the setup (cathode chamber, bubble column and all tubing in the recirculation loop) was 15 mL. To keep the reactors away from light, thereby avoiding phototrophic growth, and to maintain the temperature at 30 °C, the reactors were placed inside a cabinet. A figure of the complete setup can be found in S2.

2.4. MES reactor operation

The catholyte medium used in this work consisted out of the following components: 0.6 g L^{-1} NH_4Cl, 0.045 g L^{-1} $CaCl_2{\cdot}2H_2O$, 0.12 g L^{-1} $MgCl_2{\cdot}6H_2O$, 8.1 g L^{-1} KH_2PO_4, 0.9 g L^{-1} Na_2HPO_4, 4.5 g L^{-1} 2-

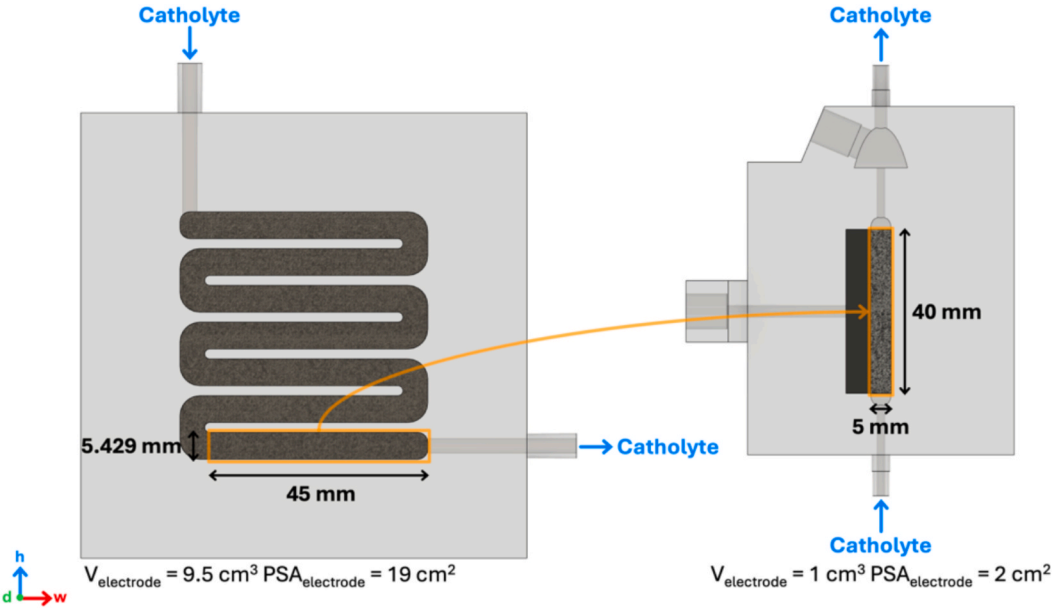

Fig. 1. Schematic representation of the cathode chamber of both the serpentine directed-flow-through bioelectrochemical reactor (DFBR) and the miniaturised DFBR, along with the corresponding sizes.

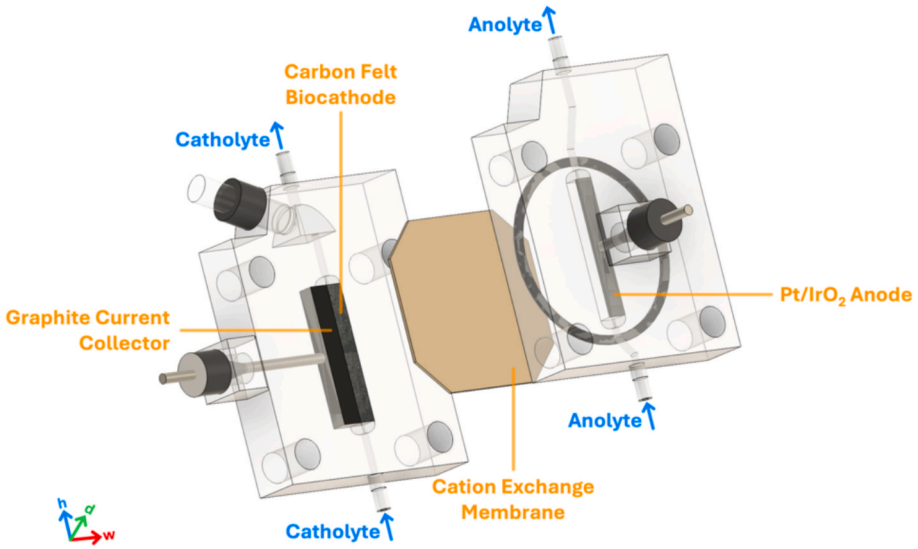

Fig. 2. Diagram of the complete reactor cell consisting of a 3D carbon felt biocathode with a graphite current collector on the cathode side and a free-flowing electrolyte with a Pt/IrO2 coated 2D titanium electrode on the anode side. The two chambers are separated by an NBR O-ring and a cation exchange membrane.

bromoethanesulfonic acid (BES) as methanogenic activity inhibitor and 3 mL L^{-1} of a trace elements solution [9]. The trace elements solution contained 1.5 g L^{-1} $FeCl_3{\cdot}6H_2O$, 0.15 g L^{-1} H_3BO_3, 0.03 g L^{-1} $CuSO_4{\cdot}5H_2O$, 0.18 g L^{-1} KI, 0.12 g L^{-1} $MnCl_2{\cdot}4H_2O$, 0.06 g L^{-1} $Na_2MoO_4{\cdot}2H_2O$, 0.12 g L^{-1} $ZnSO_4{\cdot}7H_2O$, 0.15 g L^{-1} $CoCl_2{\cdot}6H_2O$, 0.023 g L^{-1} $NiCl_2{\cdot}6H_2O$, and 10 g L^{-1} EDTA [9]. The anolyte medium was identical to the catholyte medium, excluding the methanogenic activity inhibitor and trace element solution. To facilitate proton diffusion over the CEM, the pH of the anolyte was decreased to 2 with phosphoric acid.

The reactors were operated in continuous mode with a hydraulic retention time (HRT) of 4 days and an anolyte and catholyte recirculation rate of 2.10 L h^{-1}. The cathodic bubble column was continuously sparged with 50:50 CO_2:N_2 at a rate of 0.05 L min^{-1} to provide the catholyte with dissolved CO_2. The reactors were connected to a multichannel potentiostat (BioLogic, France) in a three-electrode configuration to perform abiotic electrochemical tests and to control the reactors after inoculation. A 3 M Ag/AgCl reference electrode (QM710X, ProSense, The Netherlands) was installed in all reactors.

2.5. Abiotic electrochemical tests

Table 1 provides an overview of the electrochemical tests performed on the MES reactors prior to inoculation, along with the corresponding applications of the data obtained. The complete dataset used for data analysis can be found in the Data Availability section.

The electrochemically active surface area (ECSA) was determined using the method described by Morales et al. [33]. The allometric fitting proposed to determine the double layer capacitance (C_{dl}) involved fitting the data to a power-law function ($C_{dl} = a \cdot V^b$), using Python (version 3.10.13) and 'scipy.optimize.curve_fit'. To calculate the ECSA, a specific capacitance (C_s) of 0.02 mF cm^{-2} was used [34–37]. The onset potential for hydrogen evolution was identified using 'KneeLocator' from the 'kneed' package. The complete scripts, along with additional preprocessing steps and parameters, are documented in Data Availability section.

Additional abiotic electrochemical tests were performed on three different electrode configurations: 1) the graphite current collector, 2) a configuration with no graphite adhesive between the current collector and the carbon felt electrode, and 3) an undersized carbon felt electrode (4 mm x 5 mm x 40 mm) glued to the current collector using the method described in this work. Each of these setups was tested in triplicate, meaning three separate electrodes were evaluated for each experiment. All electrodes were tested in an identical additional setup, which operated in the same manner as the four bioelectrochemical reactors described earlier.

2.6. Inoculation and biotic operations

Prior to inoculation, the potential of the MES reactors was set (CA) at −0.9 V vs. SHE. Each reactor was inoculated with ± 9.36 mg L^{-1} of

Table 1
Abiotic electrochemical tests performed on four microbial electrosynthesis reactors with the relevant settings and measurement purpose.

Electrochemical Technique	*Settings*	*Purpose of Measurement*
CA (chronoamperometry)	• −0.9 V vs. SHE • 20 min	Polarisation of the electrode
CV (cyclic voltammetry)	• 0 to −1.2 V vs. SHE • 20 mV s^{-1} • 5 cycles	Cleaning of the electrode surface
CV (multiple scan rates)	• 0 to −0.4 V vs. SHE • 1, 20, 40, 60, 80 and 100 mV s^{-1} • 5 cycles	Determination of the electrochemically active surface area (ECSA)
CV	• 0 to −1.2 V vs. SHE • 1 mV s^{-1} • 5 cycles	Electrode kinetics
Polarisation curve	• 0 V vs. SHE to −1.2 V vs. SHE (all potential steps and durations provided in S3)	Electrode kinetics
CA	• −0.9 V vs. SHE • 24 h	System stability check

biomass consisting out of a mixed microbial culture, originating from previously operational MES reactors which produced acetate, *n*-butyrate, and *n*-caproate from CO_2 [9,38].

2.7. Analytical methods

To monitor biofilm growth and product formation, 1.5 mL of liquid samples were collected from each reactor twice a week. The optical density (OD) of unfiltered samples was measured at 600 nm using a UV–VIS spectrophotometer (UV-1800 series, Shimadzu, Japan) to account for planktonic cells. To determine biomass-specific growth rates, biomass concentrations and biomass-specific productivity as described by Winkelhorst et al. [38], the total nitrogen (TN) content of a centrifuged sample (20 min, 13300 rpm) was determined using a TOC analyser coupled with a TN unit (TOC-L Series Total Organic Carbon Analysers, Shimadzu, Japan). The oven temperature of the TOC-L with TN module was maintained at 720 °C.

The concentration of C2-C6 carboxylic acids and alcohols was determined with a gas chromatograph (Thermofisher, USA), employed with a Stabil-wax^{TM} column (25 m long and 0.2 μm internal diameter). The column temperature was held at 50 °C for 7 min, increased to 180 °C over 8 min and kept at this temperature for 9 min. The presence of methane was tested by sporadically sampling gas from the bubble column of the cathode loop and injecting the sample into a CompactGC4.0 (Global Analyser Solutions, The Netherlands). The GC was equipped with a TCD detector with He as carrier gas and a column temperature of 70 °C. Helium was used as the carrier gas at a flow rate of 1 mL min^{-1} and the ionization detector was kept at 250 °C. Production rates were calculated following the method of Winkelhorst et al. [38].

2.8. Statistical methods

Kernel scatterplot smoothing, using the Nadaraya-Watson method, was applied to the porosity profiles from micro-CT images to visualise and assess variability within the electrodes [39]. The Nadaraya-Watson method is commonly used to smooth scattered data while preserving local patterns in the data. The method estimates a smooth curve by averaging nearby data points, weighted by a kernel function, based on their distance to the target point. Kernel density smoothing was performed in Python using 'KernelSmoother' from 'skfda.preprocessing.smoothing'. To find the optimal bandwidth, which controls the smoothness of the curve, 'SmoothingParameterSearch' from 'kfda.preprocessing.smoothing.validation' was used [39]. The residuals, defined as the distances between the dataset and the kernel smoothed data, were calculated. The variability in porosity for each electrode was quantified as the root-mean-square difference ($RMSD_{porosity}$) between the observed porosity values and the kernel-smoothed values. This metric provides a measure of the typical deviation, expressed in the same unit as the porosity (%). The full script, including additional parameters and preprocessing steps, is provided in the Data Availability section.

For each reactor, the final backward scan of the 1 mV/s CV and polarisation curve was fitted to the Gompertz function using the 'scipy.optimize.curve_fit' function in Python. By modelling each backward scan of a CV and polarisation curve with a specific mathematical equation, a metric can be defined to quantify the degree of similarity between the curves, allowing their comparison and alignment. To quantify the similarity in electrochemical behaviour between reactors, the dynamic time warping (DTW) distance was calculated for each pair of reactors using 'dtw.distance' from the 'dtaidistance' library. DTW is an algorithm for measuring the similarity between two sequences that may vary in speed or time. It identifies the optimal temporal alignment, which is a correspondence between the time indices of the two sequences, by stretching and compressing the distance measure to minimise the Euclidean distance and find the best match. The resulting DTW distance matrix was normalised to create a similarity matrix, with values ranging from 0 (no similarity) to 1 (perfect similarity). The full scripts, including all parameters and preprocessing steps, are documented in the Data Availability section.

3. Results and discussion

Replicability of a miniaturised DBFR was evaluated by comparing electrochemical characteristics, biofilm growth and production spectrum between four different reactors. A combination of micro-CT imaging, conventional electrochemical techniques and statistical analysis was used to characterise the abiotic behaviour of the reactors and elucidate which electrode parts play a crucial role in the performance of carbon-based electrodes. The abiotic electrochemical data was then used to provide more insight into the factors driving biofilm growth and the production spectrum, particularly focusing on the production of C2, C4, and C6 carboxylic acids in this novel miniaturised system.

3.1. Significant variability in porosity of carbon felt electrodes

Fig. 3 showcases an example of the 3D images of the analysed carbon felt electrodes, alongside their corresponding porosity. From the six analysed electrodes, a mean bulk porosity of 58.8 % could be determined, with the maximum and minimum porosity having a 16.0 % difference in porosity. On the other hand, the bulk porosity does not provide any insight into the variability of porosity within a single electrode. Understanding the spatial distribution and variability of porosity within electrodes is essential for comprehending the potential variability in subsequent data, as it could originate from the electrode material itself. A summary of several statistics can be found in Table 2.

The root mean square difference between the actual porosity data and the kernel smoothened data ($RMSD_{porosity}$) provides a measure for local variability and fluctuation in the data. For highly variable and noisy data, the kernel smoother will have to average out these fluctuations, potentially resulting in larger distances. In the case of no variability, where the kernel smoothed data would perfectly fit the original data, $RMSD_{porosity}$ would be 0. However, in practice, a $RMSD_{porosity}$ of 0 is unlikely, as variability and noise are almost always present in obtained data. Not only does the data visually demonstrate the variability of porosity throughout the electrode (Fig. 3 and S4), the analysis also revealed significant variability in porosity values across all electrodes. These findings suggest heterogeneous porosity distributions and variances within each electrode, which may impact their performance and reliability when employed within electrochemical cells. Carbon felt electrodes, which derive their porous nature from the bonding of diverse lengths of carbon filaments, possess a considerable internal surface area that enhances electrochemical reactors. However, the data suggests that this structural variability could affect the reliability and replicability of the data obtained from the cell, potentially leading to inconsistencies in electrochemical measurements. The degree of variability within single electrodes appears to be reasonably consistent between electrodes, with the largest and smallest $RMSD_{porosity}$ having a difference of 33.2 %. This suggests that despite the difference in average porosities and porosity profiles, the overall variability in porosity remains relatively stable between samples. It is evident that, although local porosity distributions within carbon felt electrodes may vary, the overall porous properties seem to be somewhat controlled.

3.2. Electrode characteristics influence electrochemical performance

Of the four assembled MES reactors, CVs and polarisation curves were recorded. For each reactor, the last CV backward scan and polarisation curve with the corresponding Gompertz fit can be found in Fig. 4. With an R^2 of > 0.99 for each Gompertz fit, it is clear that this function is a satisfactory model to describe the data, indicating excellent agreement between the observed data and the fitted curves.

Using the DTW algorithm, the degree of similarity in electrochemical behaviour can be quantified by generating a similarity matrix. This

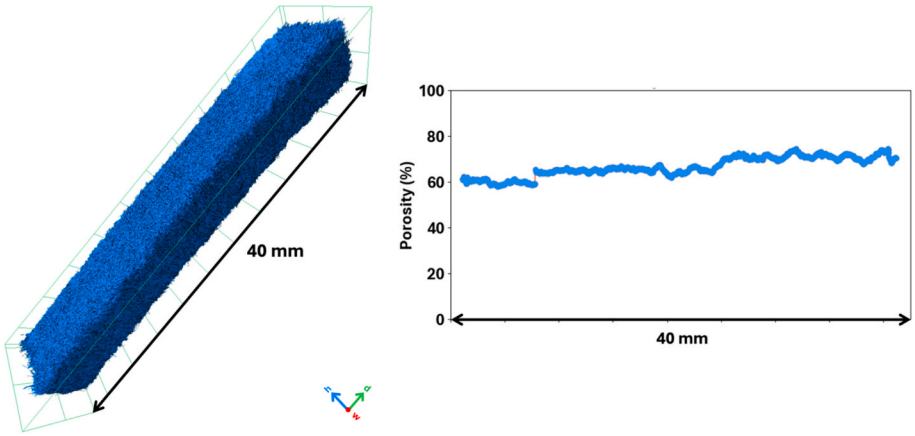

Fig. 3. 3D rendering of Electrode 1 (40 mm total height, porosity 57.97 %), generated from micro-CT data. Black areas represent the carbon fibres, while blue indicates the void spaces through which catholyte can potentially flow. The porosity profile across the electrode is also provided, with slice 0 to 1600 representing the 40 mm length of the electrode. (For interpretation of the references to colour in this figure legend, the reader is referred to the web version of this article.)

Table 2
Summary of minimum, maximum, mean, and variability in porosity for different electrodes. The variability in porosity is quantified through $RMSD_{porosity}$ (%), which represents the root-mean-square difference between the actual porosity values and the smoothed values across all data points.

	Min. Φ (%)	*Max. Φ (%)*	*Mean Φ (%)*	*$RMSD_{porosity}$ (%)*
Electrode 1	57.97	74.39	66.56	0.200
Electrode 2 (R1)	52.05	71.95	62.29	0.143
Electrode 3 (R2)	56.12	69.41	62.45	0.166
Electrode 4	43.68	59.92	52.09	0.175
Electrode 5 (R3)	40.72	63.21	50.47	0.199
Electrode 6 (R4)	52.57	67.77	59.15	0.173

similarity matrix was generated for both the last CV backward scans and the polarisation curves (Fig. 5). The matrices with the actual DTW distance between reactors can be found in S5.

The similarity scores in the matrices show minimal differences between the two electrochemical techniques and similar trends, highlighting the reliability of the method. For both techniques, reactor 2 is the most dissimilar, exhibiting the lowest similarity scores with the three other reactors. This is further supported by the CV and polarisation curve data, with reactor 2 showing a later onset potential for hydrogen evolution (Table 3) and achieving a higher current density at a final potential of −1.4 V vs. SHE.

Relating this difference to electrode porosity, the average porosity of the electrode in reactor 2 (62.5 %) is comparable to that of the electrode in reactor 1 (62.3 %), suggesting that average porosity alone may not fully capture the complexities related to an electrode's electrochemical performance. The structuring of the fibrous carbon filaments determines the flow pattern and mass transport phenomena within the porous electrode, thereby increasing some areas' exposure to the catholyte while blocking others due to pressure effects. These pressure effects are known to influence the electrical resistivity observed in carbon felt electrodes in various fields of application [40–44]. In addition, carbon felt electrodes are known to exhibit complex mass transport, leading to non-uniform kinetics within the electrode. Specifically for CV, electrode porosity and surface roughness lead to complex diffusion domains that alter measured CVs [45–48]. This suggests that not only porosity, but also the resulting intrinsic structure of the electrode influences the electrochemical behaviour of the reactor. However, the ECSA values (Table 3) show little variation among the reactors, except for reactor 4, indicating that other factors beyond ECSA contribute to the differences in behaviour. The CVs to determine the ECSA of R4 were carried out on

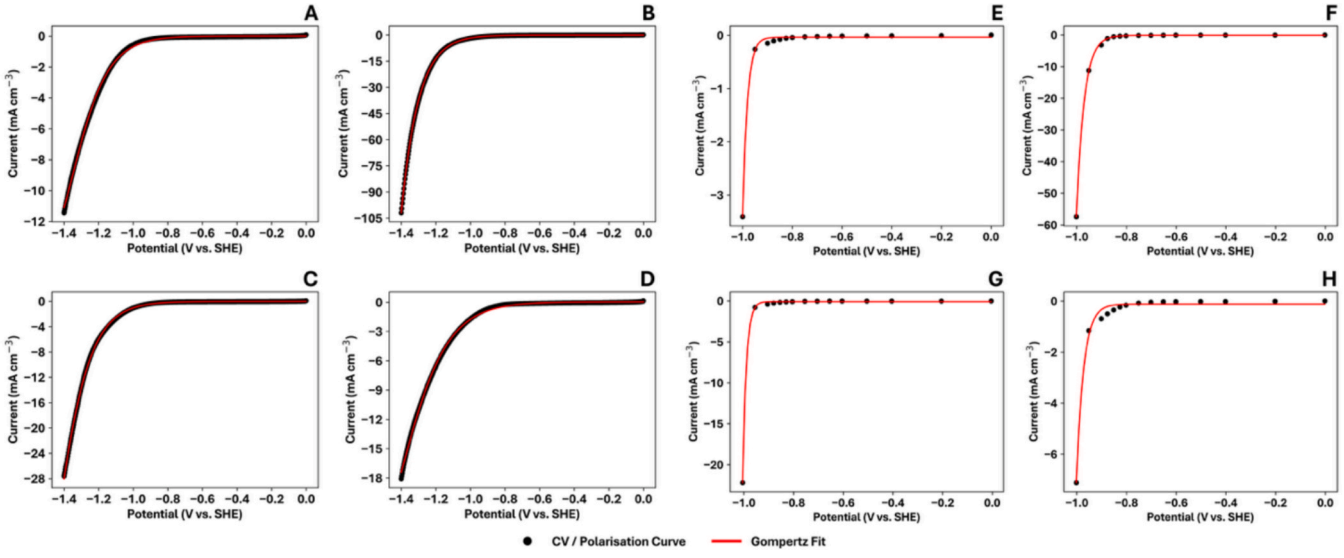

Fig. 4. Gompertz fit for the last backwards scan of a cyclic voltammogram (CV) (A-D) and polarisation curve (E-H) for reactor 1 (A, E), 2 (B, F), 3 (C, G) and 4 (D, H). For all fits, R2 > 0.99.

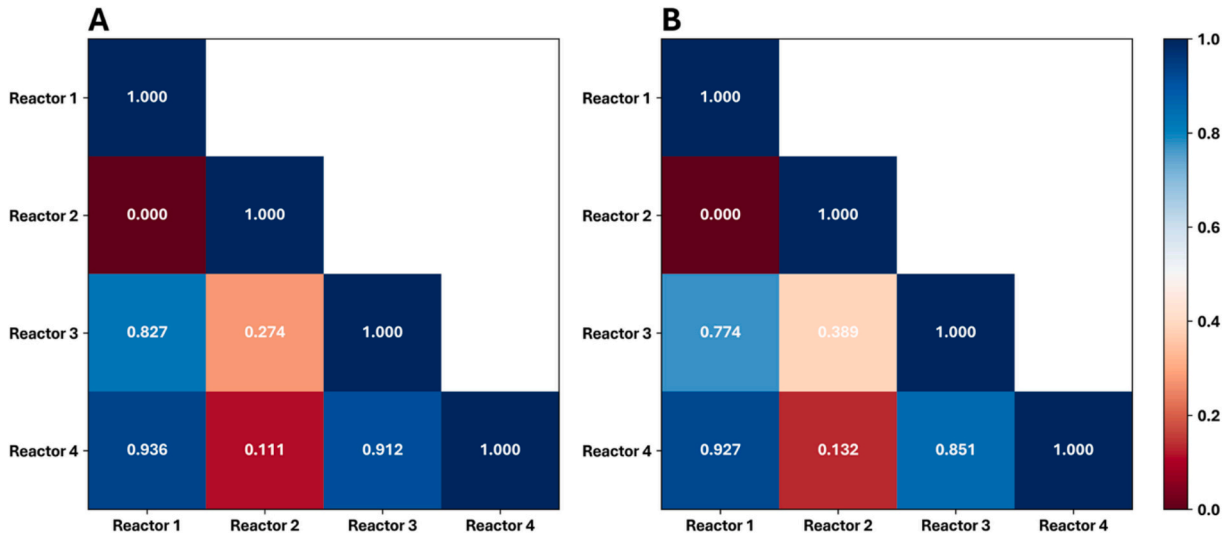

Fig. 5. Similarity matrices generated from DTW (dynamic time warping) distances between reactors using cyclic voltammetry (CV) (A) and polarisation curves (B).

Table 3
Onset potentials for H_2 evolution (V vs. SHE) determined by cyclic voltammograms (CVs) and polarisation curves for the four operated abiotic microbial electrosynthesis reactors, along with the electrochemically active surface area (ECSA).

Reactor No.	*Onset Potential H_2 Evolution CV (V vs. SHE)*	*Onset Potential H_2 Evolution Polarisation Curve (V vs. SHE)*	*ECSA (cm^2)*
1	−1.047	−0.950	320.78
2	−1.151	−0.877	349.18
3	−1.092	−0.955	378.03
4	−1.018	−0.877	627.80

the exact day the electrode was inserted into the reactor, while the electrodes in the other reactors had already been tested on for a week. This would suggest that the ECSA deteriorates over time. However, based on the data presented, such a claim is unfounded, as more data (over time) would be required. These findings indicate that factors beyond electrode structure and ECSA may contribute to the observed differences in electrochemical performance, which are further explored in the subsequent section.

3.3. Graphite conductive adhesive and electrode size are a main source of electrochemical variability

To test the validity of the methods used in this work to assemble the graphite plate and the carbon felt electrode and to investigate potential sources of variability, additional abiotic experiments were performed with either 1) only the current collector, 2) no graphite glue between the current collector and the carbon felt electrode, and 3) an undersized carbon felt electrode (which was glued to the current collector using the established method). These three conditions were selected to isolate and evaluate the specific effects of the current collector, the presence of graphite glue, and electrode size on the electrochemical performance, focusing on variables most likely to influence the system. Other configurations, such as increased electrode thickness or a thicker adhesive layer, were not tested due to pressure-related issues observed in preliminary trials. Each of the additional experiments was performed in triplicate to check replicability. The main outcomes of the additional experiments can be found in Table 4, and the data sets (CVs and polarization curves) can be found in S6.

In the experiments with the graphite plate only, the onset potential for hydrogen evolution is close to that reported for the electrodes used in this work (Table 3) as well as for the other carbon felt electrodes (NG1-3 and SE1-3). Activation overpotentials arise from the non-ideality of electrodes to catalyse an electrode reaction and represent the overpotential to initiate electron transfer. This suggests that the slow kinetics observed at the electrodes could be caused by a similarly limiting electron transfer step. Since the graphite plate is the simplest cathode setup in this case, it is probably the limiting factor in electron transfer. For the polarisation curve, the electrodes of the operational reactors show more

Table 4
Key performance indicators for the additional abiotic experiments, including the onset potential for H_2 evolution from cyclic voltammetry (CV) and polarisation curves, the maximum current density and the electrochemically active surface area (ECSA). GP: only graphite plate, NG: no glue between current collector and carbon felt electrode (1 cm^3 volume), SE: smaller carbon felt electrode of 4 mm wide (0.8 cm^3 total volume).

Reactor No.	*Onset Potential H_2 Evolution CV (V vs. SHE)*	*Onset Potential H_2 Evolution Polarisation Curve (V vs. SHE)*	*Maximum current at −1.4 V vs SHE (mA)*	*ECSA (cm^2)*
GP-1	−1.046	−1.003	−7.357	98.95
GP-2	−1.061	−1.003	−9.990	94.10
GP-3	−1.045	−0.952	−8.685	85.23
NG-1	−1.116	−0.952	−21.986	801.73
NG-2	−1.151	−1.003	−5.672	522.05
NG-3	−1.151	−1.003	−9.565	817.83
SE-1	−1.112	−0.878	−419.103	536.97
SE-2	−1.091	−0.953	−137.672	281.26
SE-3	−1.167	−1.053	−17.379	556.77

favourable and consistent onset potentials than GP1-3. This could be due to the addition of graphite adhesive to improve the connection between the graphite plate and the carbon felt electrode. Graphite adhesive is known to improve conductivity by filling gaps between surfaces and improving contact, thereby reducing electrical resistance [49].

When it comes to the maximum achievable current at −1.4 V vs. SHE, the graphite plate only setup (GP1-3) delivers the most replicable results. Since the graphite plate is a 2D electrode without surface modification and a total surface area of 2 cm^2, it was expected that similar results would be achieved between the different setups. The ECSAs for all graphite plate electrodes are also similar, but larger than the 2 cm^2 surface area available to the catholyte. Graphite is a non-porous material in its natural state unless surface modifications have been made to introduce pores. However, even without surface modification, graphite electrodes can have a larger ECSA than their geometric surface due to surface roughness, edge defects, and the presence of reactive sites, thereby enhancing their electrochemical activity [50].

Once the carbon felt electrode is placed next to the graphite plate, the maximum achievable current becomes less predictable, with values ranging from −5.672 mA cm^{-3} to −21.986 mA cm^{-3} for the carbon felt attached without graphite adhesive (NG1-3), and from −21.724 mA cm^{-3} to −523.879 mA cm^{-3} for the smaller 4 mm wide carbon felt electrodes (SE1-3). The ECSAs of the electrodes also vary more, with values generally higher than those used in the operational reactors. The reason for the higher variability in maximum current and ECSA values is unclear, but carbon adhesive could play a significant role. Graphite adhesive and other carbon-based paints are used to improve contact between conductive materials and reduce gaps that would otherwise interfere with electron flow. In addition to this, carbon paints reduce contact resistance [49]. These properties are particularly beneficial for forming a consistent conductive layer on all materials, especially when the amount of conductive adhesive used is better controlled. For the thinner electrodes, where graphite adhesive is used between the graphite current collector and the carbon felt, measurements could be less consistent due to less compression of the felt. In the operational reactors, the carbon felt is gently compressed, maximising contact between the felt, conductive adhesive and current collector. This consistent contact reduces the variability in current distribution and stabilises electron transfer between the different components. The thinner electrodes could have irregular contact points, which could lead to fluctuations in conductivity. Although the graphite adhesive and compressed carbon felt electrode result in more consistent measurements, it leads to significantly lower ECSA values than those reported for NG1-3 and SE1-3. This is likely due to the graphite adhesive filling gaps in the carbon felt near the current collector surface and additional space closing through felt compression, reducing the surface area.

The addition of graphite adhesive in the operational reactors improved the conductivity and consistency of the electrodes, leading to more favourable onset potentials and reduced electrical resistance. However, the use of thinner electrodes with graphite adhesive resulted in less predictable maximum achievable currents and higher variability in ECSA values. This suggests that optimal compression and contact between the carbon felt, adhesive, and current collector play a crucial role in the performance of carbon-based electrodes.

3.4. *Miniaturised MES supports biofilm formation and production of nC2-nC6 carboxylates*

After abiotic electrochemical characterisation, the four assembled miniaturised DFBR reactors were inoculated with an anaerobic mixed microbial culture. The composition of this mixed microbial culture can be found in S7. The cathode potential remained constant at −0.9 V vs. SHE throughout operation (105 days). The reactors were operated in continuous mode, which included continuous nutrient replenishment with a hydraulic retention time of 4 days, supplemented by continuous sparging of CO_2. Even though 4 reactors were inoculated in total, due to practical issues during inoculation only two bioreactors were operated (reactor 2 and reactor 3).

In order to follow biofilm formation, time-dependent biomass-specific growth rates (μ) were determined experimentally for both reactors (Fig. 6A) using a method proposed by Winkelhorst et al. [38]. Using biofilm development per electrode volume over time and the maximum biofilm density as described in Cabau-Peinado et al. (~12 mmol $cm^{-3}_{electrode}$), the percentage of colonised electrode could be monitored (Fig. 6B) [9]. Immediately after inoculation, up to about 50 days, both reactors show higher growth rates between 0.02 d^{-1} and 0.12 d^{-1}. From day 50 onwards, the growth rate appears to gradually decrease, reaching growth rates closer to 0.01 d^{-1}. Similar trends in biofilm growth rates were reported for both the unoptimised flow MES reactors and the serpentine DFBR [9,38]. In fact, Cabau-Peinado et al. reported that up to 225 days were required to achieve full colonisation of the electrode, even at lower current densities (~7.8 mA cm^{-3}), suggesting that slow biofilm formation is not solely linked to the electrochemical environment [9]. After 106 days of operation, a biofilm concentration of 8.74 mmol $cm^{-3}_{electrode}$ and 11.45 mmol $cm^{-3}_{electrode}$ was determined for reactor 2 and 3. Considering the maximum biofilm density of 12 mmol $cm^{-3}_{electrode}$, reactor 2 achieved 72.8 % electrode coverage by biofilm, while reactor 3 reached 95.4 %. Not only is there a clear difference between the reactors, but it also appears that the time required to achieve complete biofilm coverage of the electrodes will be shorter than the time

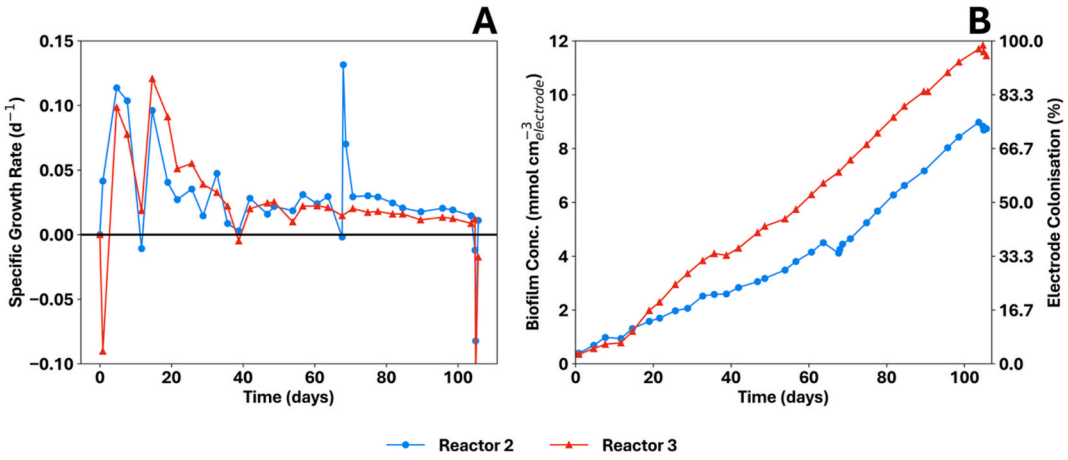

Fig. 6. (A) Biomass specific growth rates, determined with the nitrogen balancing method [37], for reactor 2 (blue circles) and reactor 3 (red triangles), (B) biofilm concentration measured over time for reactor 2 (blue circles) and reactor 3 (red triangles). (For interpretation of the references to colour in this figure legend, the reader is referred to the web version of this article.)

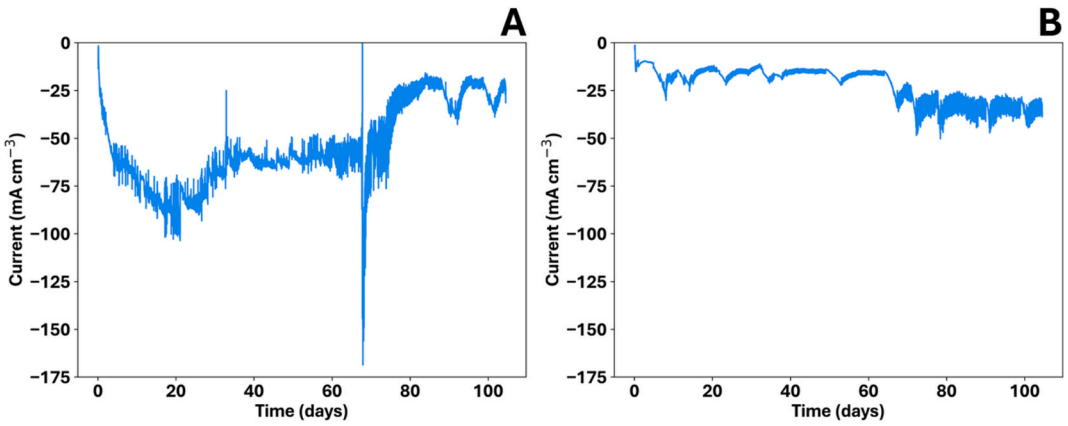

Fig. 7. Current density (normalised to electrode volume) over the 105 days of microbial electrosynthesis operation for reactor 2 (A) and reactor 3 (B).

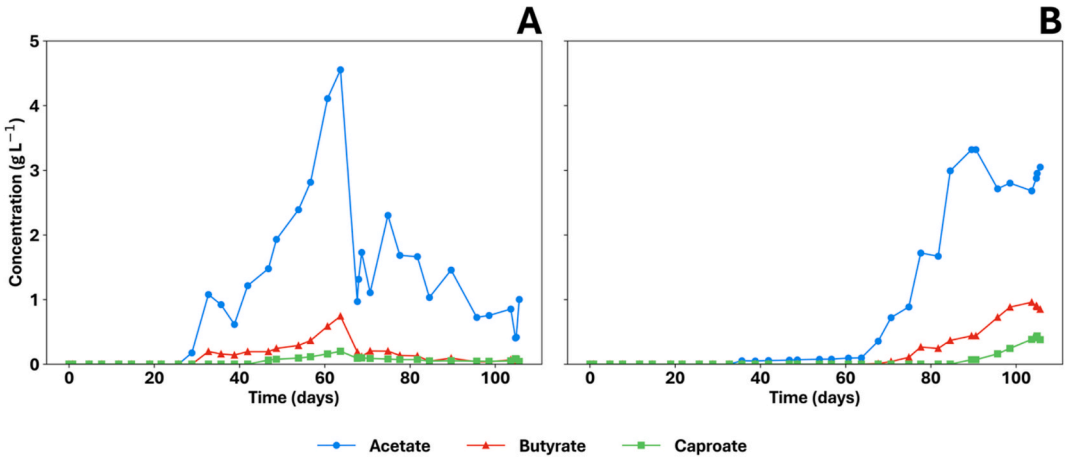

Fig. 8. Concentration (g L^{-1}) of acetate (blue circles), butyrate (red triangles) and caproate (green squares) over the 105 days of operation for reactor 2 (A) and reactor 3 (B). (For interpretation of the references to colour in this figure legend, the reader is referred to the web version of this article.)

reported for the state-of-the-art (225 days) [9]. This comparison supports the idea that factors beyond local current density, such as microbial attachment kinetics, mass transport limitations, or inoculum-specific characteristics, are likely to play a key role in biofilm development in flow-through MES systems.

The current density (Fig. 7), organics concentration (Fig. 8), production rates of products (Table 5 and S8) and faradaic efficiency (FE) (S9) were monitored for the inoculated reactors. Prior to inoculation, the current densities of both reactor 2 and 3 were similar, being around −2.10 mA cm^{-3} and −1.70 mA cm^{-3}. After inoculation, the current density changed drastically over time, with reactor 2 and 3 reaching maximum currents around −90 mA cm^{-3} and −40 mA cm^{-3}. This increase in current following inoculation, well beyond the measured currents before inoculation, is consistent with biologically driven electron uptake and biofilm formation (Fig. 6). The current becoming more negative is a common trend after inoculation in MES, as microbes use the electrons provided by the electrode to support their metabolism. However, why the cathodic current increased to such high values remains uncertain, although it could be related to the interaction of R2′s higher porosity and the less negative onset potential, which facilitates electron flow. After a pH crash (where the pH dropped below 2) on day 67, the current from reactor 2 became more positive and started fluctuating between −20 mA cm^{-3} and −40 mA cm^{-3}, making it more comparable to the current observed for reactor 3. These current densities are somewhat comparable to the current densities observed in the state-of-the-art serpentine DFBR, which reached currents between −40 mA cm^{-3} and −60 mA cm^{-3} at its peak [9].

Looking back at the abiotic electrochemistry of R2 and R3, some trends that could explain the difference in biofilm growth can be found. Firstly, from Fig. 7 it can be seen that R2 has a higher maximum current density (> −70 mA cm^{-3}) compared to R3 (~ −25 mA cm^{-3}) after inoculation. R2 also has a less negative onset potential (−0.877 V vs SHE) compared to R3 (−0.955 V vs SHE). Higher current suggests greater electron flow, which could limit biomass growth due to increased localised energy dissipation or increased hydrogen generation. The higher porosity of R2 (62.45 %) could allow for better diffusion of gases and nutrients, potentially favouring electrochemical activity over biomass growth. Conversely, lower porosity in R3 (50.47 %) might restrict electrochemical performance but create a more favourable microenvironment for biomass accumulation. These results suggest that R2′s conditions (higher current, less negative onset potential and higher porosity) favour electrochemical performance, possibly at the expense of biomass growth. In contrast, R3′s lower current, more negative onset potential and lower porosity create conditions more conducive to biomass attachment and growth.

As observed in previously operated MES reactors, the operated reactors exhibited a lag phase of 25–30 days before measurable concentrations of soluble organics were produced (Fig. 8) [9,26,38]. For both reactors, the initial product detected was acetate (C2). In the case of reactor 3, it even took up to 64 days before the acetate concentration increased significantly. Several hypotheses that deserve further investigations could explain why MES reactors consistently take around 30 days to start up, including microbial recovery after storage at low temperatures, adaptation to the new environment, community

dynamics, and medium limitations. Assuming that acetogenic species utilise the Wood-Ljungdahl pathway (WLP) for acetate production, it is known that several metalloenzymes are involved in the WLP that use selenium (Se) and tungsten (W) as co-factors, which have been shown to improve the activity of this pathway [51–53]. These metals were not added to the catholyte medium and therefore could limit microbial metabolism.

In reactor 2, shortly after the detection of acetate, butyrate (C4) was produced, which occurred about four days later. In reactor 3 the production of butyrate took longer after the detection of acetate, almost 35 days. In previous studies, an apparent C2 threshold concentration of 2–4 g L^{-1} needed to be reached before nC4 production started [12]. However, the concentration at which C4 production significantly increased in this work was closer to 1 g L^{-1}, which relates more to the values reported in Cabau-Peinado et al. [9]. For both reactors, it took 15–20 days after the first detection of butyrate to observe the production of caproate (C6). Reactor 2 experienced a pH crash on day 67, where the pH dropped to below 2, resulting in a decline in concentration of all carboxylic acids. However, production of organics resumed not long after the crash, showing the robustness of the system and the biofilm. The maximum concentrations of C2-C6 reached, including maximum production rates, are provided in Table 5. The observed trends of organic acid concentration are similar to those reported for the serpentine DFBR, however, earlier chain elongation and higher organics concentrations are observed in the first 105 days of the miniaturised DFBR. Additionally, even though the abiotic electrochemistry is considerably different between the two reactors, maximum product concentrations and production rates are comparable between the two reactors, suggesting that the mixed microbial culture can adapt to different electrochemical environments while maintaining metabolic functionality and activity.

In the approximately 30 days during which only biofilm growth was observed, and no organics were produced in either reactor, the FE for growth remained below 5 % (S9), which is considerably lower than the FEs observed in the serpentine DFBR. Even after accounting for the production of organics once they were detected, less than 10 % of the electrons supplied to the system could be dedicated to either biomass or product formation. This means that the miniaturised system has a higher dissipation of energy, as a lower FE corresponds to reduced energy efficiency. A low FE could have several reasons. For example, more H_2 production does not necessarily correspond to higher VFAs concentrations and may result in low FE due to insufficient H_2 utilisation by the biofilm. The system could also be generating unintended by-products, such as methane. Not only did the inoculum contain methanogenic species (see S7), methane concentrations of up to almost 300 ppm were detected in the headspace of the reactors, even though sodium-bromoethanesulfonate (BrES) was added to the system. Some methanogens can adapt to BrES, suggesting that administration of BrES could increase the growth and persistence of BrES-resistant methanogens [54]. Another study observed that addition of BrES does not guarantee the suppression of methanogenic species, as sulphate reducing bacteria have been demonstrated to be able to consume BrES [55,56]. Better control over the undesirable reactions occurring in an MES system is therefore considered crucial to achieve higher FEs.

Table 5
Maximum concentration of organics (acetate, butyrate and caproate) and maximum production rates (normalised to total catholyte volume) reached over the 105 days of operation for reactor 2 and reactor 3.

Reactor	*Compound*	*Maximum Concentration ($g\ L^{-1}$)*	*Maximum Production Rate ($g\ L^{-1}\ d^{-1}$)*
R2	Acetate (C2)	4.55	1.35
	Butyrate (C4)	0.74	0.24
	Caproate (C6)	0.20	0.06
R3	Acetate (C2)	3.32	1.19
	Butyrate (C4)	0.96	0.14
	Caproate (C6)	0.44	0.13

4. Conclusions

This study introduced a novel miniaturised reactor design intended to be representative of the larger, state-of-the-art serpentine DFBR. Micro-CT imaging data and abiotic electrochemical tests showed that the electrode commonly used in MES, carbon felt, leads to high variability in electrochemical performance. Kernel density regression and DTW have been introduced as reliable measures to draw conclusions about the similarity of performance between reactors. Further abiotic experiments show that the connection between current collector and electrode is important to obtain more consistent data, with the absence of graphite adhesive and a thinner electrode leading to greater differences between replicates. Variations in abiotic electrochemical conditions, such as current density, onset potential, and porosity, appear to influence biofilm growth and electrochemical performance. Nevertheless, the system achieves comparable product concentrations and production rates, indicating a balance between electrochemical activity and microbial adaptation to distinct microenvironments. Furthermore, based on biomass-specific growth rates, biofilm coverage, and organic acid (acetate, butyrate and caproate) production, the miniaturised DFBR has shown to be a good representative of the serpentine DFBR.

The presented adaptable reactor design and proposed statistical methods establish a new benchmark for future MES research, equipping researchers with tools to gain deeper insights into MES fundamentals. Nonetheless, further research is necessary to accelerate biofilm growth, improve electrode coverage, and achieve maximum productivity more efficiently in the miniaturised DFBR. This could involve exploring different electrode materials or surface modifications to enhance biofilm attachment, optimising operational conditions such as temperature, pH, and medium composition, or investigating microbial community dynamics to promote more efficient bioelectrochemical processes. Additionally, integration of real-time monitoring and data analytics could help identify key factors limiting performance and enable more targeted improvements. By representing larger, scalable state-of-the-art MES reactors, the presented miniaturised reactor provides a robust platform for such investigations, enabling faster and more detailed experimentation under controlled conditions, while requiring less resources.

5. Glossary

Microbial electrosynthesis (MES): An electricity-driven process where microorganisms derive electrons from the cathode and reduce carbon waste, such as CO_2, into valuable chemicals.

Biofilm: One or more layers of microorganisms that adhere to each other and often to a solid surface (e.g., an electrode).

Cyclic voltammetry (CV): A widely used electrochemical technique in which the current response of an electrode is measured as its potential is cycled linearly between two set values.

Chronoamperometry (CA): An electrochemical technique in which the current is measured over time in response to a sudden and sustained potential step applied to the electrode.

Polarisation curve: A current–potential curve, particularly those obtained under steady-state conditions, that provides insights into the performance of an electrochemical system.

Electrochemical active surface area (ECSA): The total surface area of an electrode that is actively involved in electrochemical reactions.

Current density: The amount of electric current passing through a unit area (or volume) of a material, such as an electrode, membrane, or reactor.

Faradaic efficiency: The selectivity of a (bio)electrochemical process, defined as the quantity (in moles) of the collected product relative to the theoretical amount producible from the total charge passed, expressed as a fraction or percentage.

CRediT authorship contribution statement

Marika A.J. Zegers: Writing – review & editing, Writing – original draft, Visualization, Validation, Software, Project administration, Methodology, Investigation, Formal analysis, Data curation, Conceptualization. **Eva Augustijn:** Validation, Methodology, Investigation. **Geurt Jongbloed:** Writing – review & editing, Formal analysis. **Ludovic Jourdin:** Writing – review & editing, Supervision, Resources, Project administration, Funding acquisition, Conceptualization.

Declaration of competing interest

The authors declare that they have no known competing financial interests or personal relationships that could have appeared to influence the work reported in this paper.

Acknowledgements

Nick Bowring and Marijn Winkelhorst are acknowledged for taking the first initiative and steps towards the development of the miniaturised microbial electrosynthesis reactor and bubble column in the lab. Appreciation is also extended to Ellen Meijvogel-de Koning for assistance with micro-CT imaging.

Funding sources

This project is funded by the Department of Biotechnology of Delft University of Technology as part of the Zero Emission Biotechnology programme.

Appendix A. Supplementary data

Supplementary data to this article can be found online at https://doi.org/10.1016/j.cej.2025.163881.

Data availability

The analysed data and full scripts for ECSA determination, onset potential determination, micro-CT data analysis and DTW distance calculation are openly available on 4TU. ResearchData at http://doi.org/10.4121/2d14c7a1-e707-4adb-939d-1556a19d9f76. All relevant parameters and preprocessing steps are also included.

References

[1] J.A. Martens, A. Bogaerts, N. De Kimpe, P.A. Jacobs, G.B. Marin, K. Rabaey, M. Saeys, S. Verhelst, The Chemical Route to a Carbon Dioxide Neutral World, ChemSusChem 10 (2017), https://doi.org/10.1002/cssc.201601051.
[2] K. Van Kranenburg, E. Schols, H. Gelevert, R. De Kler, Y. Van Delft, M. Weeda, Empowering the chemical industry, Opportunities for electrification, Tno-Ecn, 2016.
[3] N.S. Lewis, D.G. Nocera, Powering the planet: Chemical challenges in solar energy utilization, PNAS 103 (2006), https://doi.org/10.1073/pnas.0603395103.
[4] K. Rabaey, R.A. Rozendal, Microbial electrosynthesis — revisiting the electrical route for microbial production, Nat. Rev. Microbiol. 8 (2010) 706–716, https://doi.org/10.1038/nrmicro2422.
[5] D.R. Lovley, K.P. Nevin, Electrobiocommodities: powering microbial production of fuels and commodity chemicals from carbon dioxide with electricity, Curr. Opin. Biotechnol. 24 (2013) 385–390, https://doi.org/10.1016/j.copbio.2013.02.012.
[6] L. Jourdin, T. Burdyny, Microbial Electrosynthesis: Where Do We Go from Here? Trends Biotechnol. 39 (2021) 359–369, https://doi.org/10.1016/j.tibtech.2020.10.014.
[7] N.J. Claassens, C.A.R. Cotton, D. Kopljar, A. Bar-Even, Making quantitative sense of electromicrobial production, Nature Catalysis 2019 2:5 2 (2019) 437–447. Doi: 10.1038/s41929-019-0272-0.
[8] L. Jourdin, M. Winkelhorst, B. Rawls, C.J.N. Buisman, D.P.B.T.B. Strik, Enhanced selectivity to butyrate and caproate above acetate in continuous bioelectrochemical chain elongation from CO_2: Steering with CO_2 loading rate and hydraulic retention time, Bioresour. Technol. Rep. 7 (2019) 100284, https://doi.org/10.1016/j.biteb.2019.100284.
[9] O. Cabau-Peinado, M. Winkelhorst, R. Stroek, R. de Kat Angelino, A.J.J. Straathof, K. Masania, J.M. Daran, L. Jourdin, Microbial electrosynthesis from CO2 reaches productivity of syngas and chain elongation fermentations, Trends Biotechnol. (2024), https://doi.org/10.1016/J.TIBTECH.2024.06.005.
[10] V. Flexer, L. Jourdin, Purposely designed hierarchical porous electrodes for high rate microbial electrosynthesis of acetate from carbon dioxide, Acc. Chem. Res. 53 (2020) 311–321, https://doi.org/10.1021/acs.accounts.9b00523.
[11] I. Vassilev, P.A. Hernandez, P. Batlle-Vilanova, S. Freguia, J.O. Krömer, J. Keller, P. Ledezma, B. Virdis, Microbial Electrosynthesis of Isobutyric, Butyric, Caproic Acids, and Corresponding Alcohols from Carbon Dioxide, ACS Sustain. Chem. Eng. 6 (2018) 8485–8493, https://doi.org/10.1021/acssuschemeng.8b00739.
[12] L. Jourdin, S.M.T. Raes, C.J.N. Buisman, D.P.B.T.B. Strik, Critical Biofilm Growth throughout Unmodified Carbon Felts Allows Continuous Bioelectrochemical Chain Elongation from CO_2 up to Caproate at High Current Density, Front Energy Res. 6 (2018). Doi: 10.3389/fenrg.2018.00007.
[13] F. Enzmann, F. Mayer, M. Stöckl, K.M. Mangold, R. Hommel, D. Holtmann, Transferring bioelectrochemical processes from H-cells to a scalable bubble column reactor, Chem. Eng. Sci. 193 (2019), https://doi.org/10.1016/j.ces.2018.08.056.
[14] M.F. Alqahtani, K.P. Katuri, S. Bajracharya, Y. Yu, Z. Lai, P.E. Saikaly, Porous hollow fiber nickel electrodes for effective supply and reduction of carbon dioxide to methane through microbial electrosynthesis, Adv. Funct. Mater. 28 (2018), https://doi.org/10.1002/adfm.201804860.
[15] N. Chu, D. Wang, H. Wang, Q. Liang, J. Chang, Y. Gao, Y. Jiang, R.J. Zeng, Flow-electrode microbial electrosynthesis for increasing production rates and lowering energy consumption, Engineering 25 (2023), https://doi.org/10.1016/j.eng.2021.09.015.
[16] J.S. Deutzmann, G. Callander, A.M. Spormann, Improved reactor design enables productivity of microbial electrosynthesis on par with classical biotechnology, Bioresour. Technol. 416 (2025) 131733, https://doi.org/10.1016/j.biortech.2024.131733.
[17] I. Ieropoulos, J. Greenman, C. Melhuish, Improved energy output levels from small-scale Microbial Fuel Cells, Bioelectrochemistry 78 (2010), https://doi.org/10.1016/j.bioelechem.2009.05.009.
[18] G. Papaharalabos, J. Greenman, C. Melhuish, C. Santoro, P. Cristiani, B. Li, I. Ieropoulos, Increased power output from micro porous layer (MPL) cathode microbial fuel cells (MFC), Int. J. Hydrogen Energy (2013), https://doi.org/10.1016/j.ijhydene.2013.05.138.
[19] C.P.B. Siu, M. Chiao, A microfabricated PDMS microbial fuel cell, J. Microelectromech. Syst. 17 (2008), https://doi.org/10.1109/JMEMS.2008.2006816.
[20] S. Choi, J. Chae, An array of microliter-sized microbial fuel cells generating 100μW of power, Sens Actuators A Phys 177 (2012) 10–15, https://doi.org/10.1016/j.sna.2011.07.020.
[21] C.I. Torres, A.K. Marcus, B.E. Rittmann, Proton transport inside the biofilm limits electrical current generation by anode-respiring bacteria, Biotechnol. Bioeng. 100 (2008), https://doi.org/10.1002/bit.21821.
[22] J. wook Lee, E. Kjeang, A perspective on microfluidic biofuel cells, Biomicrofluidics 4 (2010), https://doi.org/10.1063/1.3515523.
[23] M.D. Yates, L.J. Bird, B.J. Eddie, E.L. Onderko, C.A. Voigt, S.M. Glaven, Nanoliter scale electrochemistry of natural and engineered electroactive bacteria, Bioelectrochemistry 137 (2021), https://doi.org/10.1016/j.bioelechem.2020.107644.
[24] T.R. Molderez, A. Prévoteau, F. Ceyssens, M. Verhelst, K. Rabaey, A chip-based 128-channel potentiostat for high-throughput studies of bioelectrochemical systems: Optimal electrode potentials for anodic biofilms, Biosens. Bioelectron. 174 (2021), https://doi.org/10.1016/j.bios.2020.112813.
[25] A. Gemünde, J. Gail, J. Janek, D. Holtmann, e-Cuvettes parallelize electrochemical and photometric measurements in cuvettes and facilitate applications in bio-electrochemistry, Biosens. Bioelectron.: X 14 (2023), https://doi.org/10.1016/j.biosx.2023.100378.
[26] M. Romans-Casas, L. Feliu-Paradeda, M. Tedesco, H.V.M. Hamelers, L. Bañeras, M. D. Balaguer, S. Puig, P. Dessì, Selective butyric acid production from CO_2 and its upgrade to butanol in microbial electrosynthesis cells, Environ. Sci. Ecotechnol. (2023) 100303, https://doi.org/10.1016/J.ESE.2023.100303.
[27] S. Bajracharya, R. Yuliasni, K. Vanbroekhoven, C.J.N. Buisman, D.P.B.T.B. Strik, D. Pant, Long-term operation of microbial electrosynthesis cell reducing CO2 to multi-carbon chemicals with a mixed culture avoiding methanogenesis, Bioelectrochemistry 113 (2017), https://doi.org/10.1016/j.bioelechem.2016.09.001.
[28] C.W. Marshall, D.E. Ross, E.B. Fichot, R.S. Norman, H.D. May, Long-term operation of microbial electrosynthesis systems improves acetate production by autotrophic microbiomes, Environ. Sci. Tech. 47 (2013) 6023–6029, https://doi.org/10.1021/ES400341B/SUPPL_FILE/ES400341B_SI_001.PDF.
[29] J.B.A. Arends, S.A. Patil, H. Roume, K. Rabaey, Continuous long-term electricity-driven bioproduction of carboxylates and isopropanol from CO2 with a mixed microbial community, J. CO_2 Util. 20 (2017), https://doi.org/10.1016/j.jcou.2017.04.014.
[30] E.V. LaBelle, H.D. May, Energy efficiency and productivity enhancement of microbial electrosynthesis of acetate, Front. Microbiol. 8 (2017), https://doi.org/10.3389/fmicb.2017.00756.
[31] P. Batlle-Vilanova, R. Ganigué, S. Ramió-Pujol, L. Bañeras, G. Jiménez, M. Hidalgo, M.D. Balaguer, J. Colprim, S. Puig, Microbial electrosynthesis of butyrate from carbon dioxide: Production and extraction, Bioelectrochemistry 117 (2017) 57–64, https://doi.org/10.1016/j.bioelechem.2017.06.004.
[32] S.M.T. Raes, L. Jourdin, C.J.N. Buisman, D.P.B.T.B. Strik, Continuous Long-Term Bioelectrochemical Chain Elongation to Butyrate, ChemElectroChem 4 (2017) 386–395, https://doi.org/10.1002/celc.201600587.

[33] D.M. Morales, M. Risch, Seven steps to reliable cyclic voltammetry measurements for the determination of double layer capacitance, J. Phys. Energy 3 (2021) 034013, https://doi.org/10.1088/2515-7655/abee33.
[34] A. Kundu, T.S. Fisher, Harnessing the thermogalvanic effect of the ferro/ferricyanide redox couple in a thermally chargeable supercapacitor, Electrochim. Acta 281 (2018), https://doi.org/10.1016/j.electacta.2018.05.164.
[35] G. Xiong, P. He, Z. Lyu, T. Chen, B. Huang, L. Chen, T.S. Fisher, Bioinspired leaves-on-branchlet hybrid carbon nanostructure for supercapacitors, Nat. Commun. 9 (2018), https://doi.org/10.1038/s41467-018-03112-3.
[36] S. Ghosh, T. Mathews, B. Gupta, A. Das, N. Gopala Krishna, M. Kamruddin, Supercapacitive vertical graphene nanosheets in aqueous electrolytes, Nano-Struct. Nano-Objects 10 (2017), https://doi.org/10.1016/j.nanoso.2017.03.008.
[37] S.K. Bikkarolla, P. Cumpson, P. Joseph, P. Papakonstantinou, Oxygen reduction reaction by electrochemically reduced graphene oxide, Faraday Discuss. 173 (2014), https://doi.org/10.1039/c4fd00088a.
[38] M. Winkelhorst, O. Cabau-Peinado, A.J.J. Straathof, L. Jourdin, Biomass-specific rates as key performance indicators: A nitrogen balancing method for biofilm-based electrochemical conversion, Front. Bioeng. Biotechnol. 11 (2023), https://doi.org/10.3389/fbioe.2023.1096086.
[39] W. Larry, Nonparametric Regression, in: L. Wasserman (Ed.), All of Nonparametric Statistics, Springer New York, New York, NY, 2006: pp. 61–123. Doi: 10.1007/0-387-30623-4_5.
[40] M. Averbukh, S. Lugovskoy, Theoretical description of carbon felt electrical properties affected by compression, Appl. Sci. 9 (2019) 4030, https://doi.org/10.3390/app9194030.
[41] T.-C. Chang, J.-P. Zhang, Y.-K. Fuh, Electrical, mechanical and morphological properties of compressed carbon felt electrodes in vanadium redox flow battery, J. Power Sources 245 (2014) 66–75, https://doi.org/10.1016/j.jpowsour.2013.06.018.
[42] L.F. Castañeda, F.C. Walsh, J.L. Nava, C. Ponce de León, Graphite felt as a versatile electrode material: properties, reaction environment, performance and applications, Electrochim. Acta 258 (2017) 1115–1139, https://doi.org/10.1016/j.electacta.2017.11.165.
[43] R. Banerjee, N. Bevilacqua, A. Mohseninia, B. Wiedemann, F. Wilhelm, J. Scholta, R. Zeis, Carbon felt electrodes for redox flow battery: impact of compression on transport properties, J Energy Storage 26 (2019) 100997, https://doi.org/10.1016/j.est.2019.100997.
[44] A. Gaunand, F. Coeuret, Influence of the relative electric conductivity of the two phases on the pontential distribution in flow-though porous electrodes under limiting current conditions, Electrochim. Acta 23 (1978), https://doi.org/10.1016/0013-4686(78)85072-5.
[45] L. Landon-Lane, A.J. Downard, A.T. Marshall, Single fibre electrode measurements – A versatile strategy for assessing the non-uniform kinetics at carbon felt electrodes, Electrochim. Acta 354 (2020) 136709, https://doi.org/10.1016/j.electacta.2020.136709.
[46] I. Streeter, G.G. Wildgoose, L. Shao, R.G. Compton, Cyclic voltammetry on electrode surfaces covered with porous layers: an analysis of electron transfer kinetics at single-walled carbon nanotube modified electrodes, Sens. Actuat. B Chem. 133 (2008), https://doi.org/10.1016/j.snb.2008.03.015.
[47] E.O. Barnes, X. Chen, P. Li, R.G. Compton, Voltammetry at porous electrodes: a theoretical study, J. Electroanal. Chem. 720–721 (2014), https://doi.org/10.1016/j.jelechem.2014.03.028.
[48] D. Menshykau, R.G. Compton, The influence of electrode porosity on diffusional cyclic voltammetry, Electroanalysis 20 (2008), https://doi.org/10.1002/elan.200804334.
[49] S.S. Azim, A. Satheesh, K.K. Ramu, S. Ramu, G. Venkatachari, Studies on graphite based conductive paint coatings, Prog. Org. Coat. 55 (2006), https://doi.org/10.1016/j.porgcoat.2005.09.001.
[50] M. Schalenbach, V. Selmert, A. Kretzschmar, L. Raijmakers, Y.E. Durmus, H. Tempel, R.A. Eichel, How microstructures, oxide layers, and charge transfer reactions influence double layer capacitances. Part 1: impedance spectroscopy and cyclic voltammetry to estimate electrochemically active surface areas (ECSAs), PCCP 26 (2023), https://doi.org/10.1039/d3cp04743a.
[51] X. Zhu, X. Tan, Metalloproteins/metalloenzymes for the synthesis of acetyl-CoA in the Wood-Ljungdahl pathway, Sci China B Chem 52 (2009) 2071–2082, https://doi.org/10.1007/s11426-009-0082-3.
[52] F. Ammam, P.-L. Tremblay, D.M. Lizak, T. Zhang, Effect of tungstate on acetate and ethanol production by the electrosynthetic bacterium Sporomusa ovata, Biotechnol. Biofuels 9 (2016) 163, https://doi.org/10.1186/s13068-016-0576-0.
[53] J. Saxena, R.S. Tanner, Effect of trace metals on ethanol production from synthesis gas by the ethanologenic acetogen, Clostridium ragsdalei, J. Ind. Microbiol. Biotechnol. 38 (2011) 513–521, https://doi.org/10.1007/s10295-010-0794-6.
[54] L. Rago, Y. Ruiz, J.A. Baeza, A. Guisasola, P. Cortés, Microbial community analysis in a long-term membrane-less microbial electrolysis cell with hydrogen and methane production, Bioelectrochemistry 106 (2015) 359–368, https://doi.org/10.1016/j.bioelechem.2015.06.003.
[55] B. Bian, J. Xu, K.P. Katuri, P.E. Saikaly, Resistance assessment of microbial electrosynthesis for biochemical production to changes in delivery methods and CO2 flow rates, Bioresour. Technol. 319 (2021), https://doi.org/10.1016/j.biortech.2020.124177.
[56] S. Mills, P. Dessì, D. Pant, P. Farràs, W.T. Sloan, G. Collins, U.Z. Ijaz, A meta-analysis of acetogenic and methanogenic microbiomes in microbial electrosynthesis, NPJ Biofilms Microbiom. 8 (2022) 73, https://doi.org/10.1038/s41522-022-00337-5.